Available online at www.sciencedirect.com
SCIENCE DIRECT®
Planetary and Space Science 52 (2004) 149–156
Planetary and Space Science
www.elsevier.com/locate/pss

Performance and surface scattering models for the Mars Advanced Radar for Subsurface and Ionosphere Sounding (MARSIS)

G. Picardi[a,*], D. Biccari[a], R. Seu[a], L. Marinangeli[b], W.T.K. Johnson[c], R.L. Jordan[c], J. Plaut[c], A. Safaenili[c], D.A. Gurnett[d], G.G. Ori[b], R. Orosei[e], D. Calabrese[f], E. Zampolini[f]

[a] *Infocom Department, "La Sapienza" University of Rome, Via Eudossiana, 18, 00184 Rome, Italy*
[b] *IRSPS, Università G.D'Annunzio, Viale Pindaro 42, Pescara, Italy*
[c] *Jet Propulsion Laboratory, 4800 Oak Grove Drive, Pasadena, CA 91109, USA*
[d] *Dept. of Physics and Astronomy, University of Iowa, Iowa City, IA 52242-1447 USA*
[e] *CNR/IAS, Planetology Department Via del Fosso di Cavaliere, 00133 Rome, Italy*
[f] *Alenia Spazio, Space Division, Via Saccomuro, 24-00131 Rome, Italy*

Received 2 April 2003; received in revised form 6 June 2003; accepted 29 August 2003

Abstract

The primary scientific objective of the Mars Advanced Radar for Subsurface and Ionosphere Sounding (MARSIS), which will be on board Mars Express mission scheduled for launch in 2003, is to map the distribution and depth of the liquid water/ice interface in the upper kilometres of the crust of Mars. MARSIS will also provide unique information to help us understand the recent crustal evolution of the planet. In addition an ionosphere sounding experiment will measure the electron density and structure of the upper atmosphere during day-time operations.

We describe the design approach and expected performance by focusing on a model of the surface scattering, which is critical to obtaining a good quality radar response.

We characterize the surface in terms of large-scale morphology upon which small-scale geometric variation is superposed. Moreover, MOLA data have been processed using a fractals model to better describe the surface roughness of Mars.

We used three categories of rock material with different dielectric properties to assess the performance of the Radar Sounder and detect the depth of the ice/water and dry/ice interface. This paper will focus on studying the effect of Mars surface roughness on the penetration performance of MARSIS as a subsurface sounding instrument. The impact of ionosphere on MARSIS operation and performance is significant and will be discussed in a future paper by other authors.

Keywords: Radar exploration; Mars; Subsurface; Surface scattering; Radar sounder

1. Introduction

Mars Advanced Radar for Subsurface and Ionosphere Sounding (MARSIS) is a low-frequency (0.1–5.5 MHz) nadir-looking pulse limited radar sounder and altimeter with ground penetration capabilities. It uses an unfocused synthetic aperture technique and a secondary receiving antenna to isolate subsurface reflections. MARSIS subsurface sounding mode operates at 1.3–5.5 MHz frequency range in order to maximize the penetration capabilities of the transmitted pulse. Taking into account the expected values of the plasma frequency in the Martian ionosphere, MARSIS will operate the 1.8, 3, 4 and 5 MHz frequencies.

The requirement for range resolution calls for a relatively large transmitted bandwidth in MARSIS design; a 1 MHz bandwidth provides a vertical resolution of about 150 m in vacuum which corresponds to 50–100 m in the subsurface, depending on the wave propagation speed in the crust. The typical spatial resolution of MARSIS which can be effectively operated at any altitude lower than 800 km, will be from 5–10 Km in the along track direction and from 15 to 30 km in the cross-track direction.

When a short pulse of energy is incident on the top of a surface, it produces a first (surface) reflection echo which propagates backward to the antenna. In general, a portion of

* Corresponding author.
E-mail address: picar@infocom.ing.uniroma1.it (G. Picardi).

0032-0633/$ - see front matter © 2003 Elsevier Ltd. All rights reserved.
doi:10.1016/j.pss.2003.08.020

the incident energy is transmitted through the surface and attenuated as it propagate in the medium. However, if long wavelengths are employed, a significant fraction of the energy can penetrate deeper into the crust. Additional reflections, due to the subsurface dielectric discontinuities can be generated and the resulting in echoes would propagate backward through the first layer medium to the radar antenna. These secondary echoes will be much weaker than the surface reflection. Assuming that the propagation speed in the subsurface media is known, the time delays of the echoes can be converted into penetration depths. The intensity of the reflections could also be analysed to estimate interface reflectivity and attenuation properties of the intervening layers.

The MARSIS instrument has an estimated dynamic range of 50–60 dB, but there are several factors that can strongly reduce the detection dynamic range such as the system thermal noise and galactic background. Another source of noise that can reduce the system dynamic range is the clutter. Due to the orbital sounding geometry, off-nadir surface returns or clutter noise might be received at the same time as are subsurface echoes; therefore, the echoes reflected from rough surface might totally mask the signals generated by subsurface discontinuities. As the surface becomes smoother, the return echoes from off-nadir angles will decrease. Hence, it is important to evaluate the possible penetration depths according to the transmitted wavelength, the dielectric characteristics of the crust and the surface scattering behaviour as a function of the surface roughness.

Different techniques are envisioned to increase the MARSIS detection performance in the presence of surface clutter (Picardi et al., 1999):

- *the Doppler Azimuth processing* can reduce surface clutter from along-track, off-nadir direction. The improvement on the overall surface clutter attenuation should be in the order of 10 dB.
- a *secondary antenna*, (*a monopole antenna*) oriented along the nadir axis, and which will receive mostly the off-nadir surface returns. These returns may then be subtracted from the primary antenna composite signal to further reduce the surface clutter level by about 15 dB.
- echo profiles collected at *two different bands* can be processed to separate the subsurface reflections, which are strongly dependent on the frequency, from the surface reflections, which are mostly frequency independent. The achieved improvement in signal to clutter ratio can reach 10–15 dB (Picardi et al., 1999).

2. Reference crustal model

Electromagnetic property of Mars subsurface is not known. Recent data from Mars Global Surveyor and Mars Odyssey missions have shown a rather complex surface geology of Mars. The occurrences of recent shallow water activity revealed by gullies (Malin and Edgett, 2000; Gaidos, 2001; Mellon and Phillips, 2001; Mustard et al., 2001; Costard et al., 2002; Grimm, 2003; Gilmore and Phillips, 2002) and fluvial channel reactivation, the presence of hematite deposits (Christensen et al., 2001) and the possible surface water distribution inferred from the Hydrogen abundance detected by the gamma ray spectrometer (Boynton et al., 2002), reveal the large variety of materials which may characterize the upper kilometres of the Martian crust.

Table 1
Summary of the dielectric characteristics of reference categories and pore-filling material used to test the MARSIS performances

Category	ε'	$\tan\delta$
Rock material		
I	5	0.004
II	9	0.03
III	7.1	0.014
Pore filling		
Air	1	0
Solid H_2O (ice)	3.15	0.0002
Liquid H_2O (water)	0.0088	0.0001

However, in order to evaluate the performance of MARSIS as a tool to investigate Mars subsurface, we need to assume a certain range of materials with different dielectric characteristics which may be present in the Martian subsurface. We summarized in Table 1 the three main reference categories and pore-filling material used in our modelling. The categories have been defined considering dielectric constants of terrestrial volcanic, sedimentary and metamorphic rocks found in literature.

Two different scenarios are envisioned to test the MARSIS capabilities to detect the air/water/ice transition in the Martian crust:

1. *Ice/water (I/W) interface*: The pores are filled with ice down to a depth below which liquid water is stable. The change of the pore-filling material causes a discontinuity in the dielectric constant, which can be detected by the radar sounder.
2. *Dry/ice (D/I) interface*: The pore-filling material is considered to be gas or some other vacuum-equivalent material to a depth below which ice fills the pores.

3. Fresnel coefficients and subsurface attenuation

As stated in Section 1, assuming that the propagation speed in the medium is known, the time delay of the received echo can be converted to depth. The intensity of the reflection can be used to estimate the reflectivity at any interface defined by a dielectric discontinuity, if a reference reflection is known, and to estimate the attenuation properties of the intervening layers, as well. However, the surface return echoes may reduce the visibility of the

subsurface echoes. Thus we need to evaluate the backscattering cross-sections (σ) of concurrent echoes coming both from the surface and subsurface layers in order to detect an interface. The backscatter values for the surface (σ_s) and the subsurface (σ_{ss}) can be expressed as

$$\sigma_s = \Gamma_s f_s(H_s, s_s, \lambda) \tag{1}$$

and

$$\sigma_{ss} = \Gamma_{ss} f_{ss}(H_{ss}, s_{ss}, \lambda), \tag{2}$$

where Γ_s and Γ_{ss} are the Fresnel reflectivity terms, which are related to dielectric properties, and f_s and f_{ss} the scattering terms, which deal with the geometric structure of the surface and subsurface. In the following sections we will evaluate both the Fresnel and the geometric scattering terms using the crustal properties and models shown in Table 1.

The evaluation of the Fresnel reflectivity terms requires the knowledge of the complex dielectric constants of the crustal material (ε_{r1}) and of the interface at depth (ε_{r2}). Starting from the dielectric constants of the selected categories I, II and III, and using an exponential law for the porosity variation with depth (adapting a similar model devised for the Moon, based on seismic data which are not available for Mars (Binder and Lange, 1980; Clifford, 1993), the complex dielectric constants can be evaluated using Host–Inclusion mixture models. Following the assumption that the crust porosity is a function only of the depth, we can use the Maxwell–Garnett mixing model to describe the dielectric constant of the solid/pore filling mixture (ε_m) at different depths, such that

$$\varepsilon_m(z) = \varepsilon_h \frac{1 + 2\phi(z)y}{1 - \phi(z)y}, \tag{3}$$

where ε_h is the dielectric constant of the host material and

$$y = \frac{\varepsilon_i - \varepsilon_h}{\varepsilon_i + 2\varepsilon_h}, \tag{4}$$

where ε_i is the dielectric constant of the inclusion.

The porosity at depth z is described as

$$\Phi(z) = \Phi(0)\mathrm{e}^{-z/K}, \tag{5}$$

where K is the decay constant. The decay constant for Mars can be calculated by comparison with the measured Lunar decay constant. In fact, assuming comparable crust densities between the Moon and Mars, the Martian decay constant can be calculated considering the ratio between the Lunar and Martian surface gravitational accelerations, resulting in a value of 2.8 km (Clifford, 1993).

Therefore, the *Surface Fresnel reflectivity* for a nadir incidence wave in free space is

$$\Gamma_s = \left| \frac{1 - \sqrt{\varepsilon_{r1}(0)}}{1 + \sqrt{\varepsilon_{r1}(0)}} \right|^2 = R_{01}^2, \tag{6}$$

where $\varepsilon_{r1}(0)$ is the real dielectric constant of the crust evaluated at the surface ($z = 0$).

Table 2
Fresnel reflectivity coefficients of the surface ($z = 0$) for the ice/water (I/W) and dry/ice (D/I) scenarios. The percentage represents the porosity

$\Gamma_{s\,dB}$				
	I/W		D/I	
Categories	$\Phi(0)$ 50%	$\Phi(0)$ 20%	$\Phi(0)$ 50%	$\Phi(0)$ 20%
I	−9.5	−9	−12	−9.5
II	−7.5	−6.5	−9	−7
III	−8.5	−7.5	−10	−8

Table 3
Fresnel reflectivity coefficients of the I/W and D/I interfaces at different depth

$R^2_{12,z'\,\mathrm{dB}}$				
	I/W		D/I	
Depth (m)	50%	20%	50%	20%
$z' = 0$	−10	−17	−22	−25
$z' = 1000$	−12	−20	−26	−32
$z' = 2000$	−15	−23	−28	−36
$z' = 3000$	−18	−26	−31	−38
$z' = 4000$	−21	−28	−33	−42
$z' = 5000$	−24	−31	−35	−46

The surface reflectivity values for categories I, II and III are shown in Table 2. The reflectivity values range between −7 and −17 dB for the I/W scenario and −7 and −25 dB for the D/I scenario.

The Fresnel reflectivity for a subsurface layer located at a depth z' can be expressed as follows:

$$\Gamma_{ss,z'} = R_{12,z'}^2 (1 - R_{01}^2)^2 10^{-0.1 \int_0^{z'} \alpha(z)\,\mathrm{d}z}, \tag{7}$$

where $R_{12,z'}^2$ is the reflection coefficient of the interface and is described by the formula

$$R_{12,z'}^2 = \left| \frac{\sqrt{\varepsilon_{r1}(z')} - \sqrt{\varepsilon_{r2}(z')}}{\sqrt{\varepsilon_{r1}(z')} + \sqrt{\varepsilon_{r2}(z')}} \right|^2 \tag{8}$$

and $\alpha(z)$ is the wave attenuation. The results are shown in Table 3. The reflectivity intensity at different depth varies according to the following relations:

$$\text{I/W} \quad R_{12,z'\cong}^2 - a - 3z', \quad 10 < a < 18, \tag{9}$$

$$\text{D/I} \quad R_{12,z'\cong}^2 - b - 3z' \quad 20 < b < 28, \tag{10}$$

where the first term is related to the porosity of the first layer and the latter is due to the decrease of the porosity with depth (z' [km]).

The $R_{12,z'}^2$ does not depend strongly on the crust material but mostly depends on the pore-filling material discontinuity.

Table 4
Crust attenuation vs. depth (km)

$\alpha(z)$ dB/km MHz				
I/W			D/I	
	$\Phi(0)50\%$	$\Phi(0)20\%$	$\Phi(0)50\%$	$\Phi(0)20\%$
I	$(0.8+0.1z)$	$(1.3+0.05z)$	$(0.9+0.1z)$	$(1.3+0.05z)$
III	$(3.7+0.54^*z)$	$(6+0.25^*z)$	$(4.3+0.54^*z)$	$(6.3+0.25^*z)$
II	$(8.5+1.1^*z)$	$(13.3+0.5^*z)$	$(9.5+1.1^*z)$	$(13.7+0.5^*z)$

Considering the two way attenuation:

$$\alpha_{\mathrm{dB/m}}(z) = 1.8\times 10^{-7} f_0 \sqrt{\varepsilon(z)}\tan\delta(z), \tag{11}$$

we have obtained, with good approximation, a simple analytical expression the of signal attenuation, as depth summarized in Table 4.

4. Surface backscattering models

Considering the MARSIS wavelength as the scale, we can evaluate the Martian surface backscattering (Ulaby et al., 1986) by considering two main contributions: (1) the *large-scale scattering*, resulting from gentle surface undulations on a scale of many hundreds to thousands meters, and (2) the *small-scale scattering*, resulting from slight variations of the surface height over a horizontal scale of tenths of meters. A plausible range for the parameters describing the surface geometry is listed in Table 5.

From the statistical point of view, the surface height will be modelled as a Gaussian random process, where σ_{h1} is the surface RMS height. At a second-order level we suppose an isotropic surface autocorrelation function.

Taking into account the classical studies (Ulaby et al., 1986; Fung et al., 1992) on the validity conditions of the backscattering models, the Kirchhoff theory can be used to estimate the backscattering contribution for gently undulating surfaces (large-scale models) and the Small Perturbation Method can be applied to slightly rough surfaces (small-scale model).

4.1. Large-scale (Kirchhoff) scattering evaluation

Under the hypothesis of the Kirchhoff approximation the scattered electric field towards the receiving antenna is given by the following integral (Ulaby et al., 1986):

$$E_{\mathrm{s}}(t) = \frac{1}{2\pi}\int_{-\infty}^{\infty} F(\omega)\left(-\frac{\mathrm{j}}{2\lambda}\right)\int_S G(P)R(P) \times \frac{\hat{n}\cdot(2\hat{R}_1)}{R_1^2}\mathrm{e}^{-\mathrm{j}k2R_1}\,\mathrm{d}S\mathrm{e}^{\mathrm{j}\omega t}\,\mathrm{d}\omega, \tag{12}$$

where $E_{\mathrm{i}} = (1/R_1)\mathrm{e}^{-\mathrm{j}kR_1}$ is the incident spherical wave, $k = 2\pi/\lambda$ is the wave number, λ is the wavelength, $F(\omega)$ is the Fourier transform of the transmitted pulsed waveform, P is the generic point on the surface, $G(P)$ is the normalized antenna gain in the direction of the point P on the surface S, $R(P)$ is the local (at point P) Fresnel coefficient, R_1 is the distance from the radar to the point P, $\hat{R}_1$ is the unit vector corresponding to the path from the radar to the point P, and $\hat{n}$ is the unit vector normal to the surface at the point P.

If we make the further assumption of an isotropic antenna pattern and that the surface tilt is small enough to allow to assume the nadir axis equal to the local normal to the surface, we have $G(P) = 1$ and $\hat{n}\cdot\hat{R}_1 \approx \hat{z}\cdot\hat{R}_1 = \cos\theta$, where $\theta$is the incidence angle with respect to the vertical. Moreover, the distance from the radar to the generic point $P(x, y, z)$ can be approximated, with the far-field approximation, as

$$R_1 \approx h - z\cos\theta + \frac{x^2+y^2}{2h}, \tag{13}$$

where h is the distance from the radar to the mean surface. With all these assumptions Eq. (12) becomes:

$$E_{\mathrm{s}}(\tau) = -\frac{2}{4\pi c}\frac{\cos\theta}{h^2}R(\theta)\int_{\mathrm{s}}\mathrm{d}S \times \int_{-\infty}^{\infty}\mathrm{e}^{\mathrm{j}\omega(\tau-((x^2+y^2)/hc)+(2z\cos\theta/c))}\mathrm{j}\omega F(\omega)\,\mathrm{d}\omega, \tag{14}$$

where $\tau = t-(2h/c)$ and the angle of incidence θ is assumed to undergo no significant variation within the pulse limited integration area, and has been therefore taken out of the surface integral.

The average scattered power at time τ can be computed taking the average of the product of the scattered electric field with its complex conjugate:

$$\langle E_{\mathrm{s}}(\tau)E_{\mathrm{s}}^*(\tau)\rangle = \frac{4\Gamma_{\mathrm{s}}(\theta)}{(4\pi c h^2)^2}\cos^2\theta\int\mathrm{d}\omega_1 \times \int\mathrm{d}\omega_2\omega_1\omega_2 F(\omega_1)F^*(\omega_2)\mathrm{e}^{\mathrm{j}(\omega_1-\omega_2)\tau} \times \int_{S_1}\mathrm{d}S_1\int_{S_2}\mathrm{d}S_2\mathrm{e}^{-\mathrm{j}/ch[\omega_1(x_1^2+y_1^2)-\omega_2(x_2^2+y_2^2)]} \times\langle\mathrm{e}^{\mathrm{j}(2\cos\theta/c)(\omega_1 z_1-\omega_2 z_2)}\rangle \tag{15}$$

where $\Gamma_{\mathrm{s}}(\theta) = |R(\theta)|^2$ is the Fresnel reflection coefficient. The average on the height z can be expressed as a function

Table 5
Summary of the values range for the geometric parameters of the surface

Large-scale model		Small-scale model	
RMS slope (m_s)	Correlation Length (L)	RMS Slope RMS Slope	RMS height RMS height
0.01–0.1 rad (0.57°–5.7°)	200–30,000 m	0.1–0.6 rad (5.7°–34.3°)	0.1–1 m

of the surface two-dimensional characteristic function:

$$\langle e^{j(2\cos\theta/c)(\omega_1 z_1-\omega_2 z_2)}\rangle = e^{-2\sigma_{h1}^2(\cos^2\theta/c^2)(\omega_1^2+\omega_2^2-2\rho(x_1,x_2,y_1,y_2)\omega_1\omega_2)}. \quad (16)$$

The solution of integral (15) is not trivial in the general case. A closed form has been derived (Fung and Eom, 1983) assuming a Gaussian correlation coefficient (l is the correlation length), and a Gaussian pulse spectrum which corresponds to a Gaussian shape of the compressed pulse:

$$S(j\omega) = \frac{\tau_P}{\sqrt{\pi}} e^{-\tau_P^2\omega^2} \rightarrow f(t) = e^{-(t^2/4\tau_P^2)}\cos\omega_0 t \quad (17)$$

being τ_P related to the system bandwidth B_W: $\tau_P \approx 0.37/B_W$ and then to the radar range resolution.

These assumptions lead to the following results (Ciaffone et al., 1994):

$$\langle E_s(\tau)E_s^*(\tau)\rangle = \Gamma_s(\theta)\frac{1}{4h^2}\cos^2\theta(P_c + P_{nc1} - P_{nc2}), \quad (18)$$

where $P_c(\tau)$ is the *coherent* (*specular*) scattering component:

$$P_c(\tau) = \frac{1}{1+F} e^{-(2k\sigma_{h1}\cos\theta)^2/1+F} e^{-\tau^2/2\tau_P^2(1+F)} \quad (19)$$

We define $P_{nc}(\tau) = P_{nc1}(\tau) - P_{nc2}(\tau)$ to be the *non-coherent* (*diffuse*) scattering component:

$$P_{nc1}(\tau) = \frac{\beta}{\sqrt{1+2F}}\sqrt{\frac{\pi}{2}} e^{\beta^2/2} e^{-\beta(\tau/\tau_P\sqrt{1+2F})} \times Erfc\left[\frac{1}{\sqrt{2}}\left(\beta - \frac{\tau}{\tau_P\sqrt{1+2F}}\right)\right], \quad (20)$$

$$P_{nc2}(\tau) = \frac{\beta}{\sqrt{1+F}\sqrt{1+2F}}\sqrt{\frac{\pi}{2}} e^{-(2k\sigma_{h1}\cos\theta)^2/1+F} \times e^{\beta^2(1+F)/2(1+2F)} e^{-\beta(\tau/\tau_P\sqrt{1+2F})} \times Erfc\left[\frac{1}{\sqrt{2}}\left(\beta\sqrt{\frac{1+F}{1+2F}} - \frac{\tau}{\tau_P\sqrt{1+F}}\right)\right], \quad (21)$$

where the *normalized projected roughness* (F) *is*

$$F = \frac{1}{2}\frac{\sigma_{h1}^2\cos^2\theta}{(c\tau_P/2)^2} \quad (22)$$

and the *equivalent pulse width* (τ_{eq}) is

$$\tau_{eq} = \sqrt{\tau_P^2 + \left(\frac{2\sigma_{h1}\cos\theta}{c}\right)^2} = \tau_P\sqrt{1+2F} \quad (23)$$

and the *surface parameter* (β) is

$$\beta = \frac{c\tau_P}{2H}\frac{\sqrt{1+2F}}{m_s^2\cos\theta}(1 - e^{-(2k\sigma_{h1}\cos\theta)^2}) \quad (24)$$

where m_s is the rms slope ($m_s = \sqrt{2}(\sigma_{h1}/l)$).

Therefore, the cross-section of the large-scale surface model is given by

$$\sigma_1(\tau) = \frac{\langle E_s(\tau)E_s^*(\tau)\rangle}{\langle E_i(\tau)E_i^*(\tau)\rangle}4\pi h^2 = \Gamma_s(\theta)\pi h^2\cos^2\theta(P_c + P_{nc1} - P_{nc2}). \quad (25)$$

The maximum power is received if full coherent reflection occurs, i.e. when the surface is perfectly flat ($\sigma_{h1} = 0$). In such a condition it is easy to verify that $P_{nc1} = P_{nc2}$ and the non-coherent term P_{nc} reduces to zero, while the coherent term P_c approaches the shape of the transmitted pulse, which is maximum for $\tau = 0$ so that:

$$\sigma_{1,MAX}(0) = \Gamma_s(0)\pi h^2, \quad (26)$$

which is a value consistent with the backscattering of perfectly flat surfaces. As the surface becomes rougher (σ_{h1} referred to λ) the coherent component decreases towards zero and the non-coherent scattering becomes:

$$\sigma_{1MAX,nc}(\tau) \approx \Gamma_s(0)\pi h^2\frac{\beta}{\sqrt{1+2F}}\sqrt{\frac{\pi}{2}}2e^{-\beta^2/2} \approx \Gamma_s(0)\pi h\frac{c\tau_P}{2}\sqrt{2\pi}\frac{1}{m_s^2} \approx \Gamma_s(0)\pi h\frac{c0.37}{2B_W}\sqrt{2\pi}\frac{1}{m_s^2} \approx \Gamma_s(0)\pi h\frac{c}{2B_W}\frac{1}{m_s^2} \quad (27)$$

According to the geometrical optics model, the quantity $\sqrt{2h(c/2B_W)}$ is the radius of the well-known pulse-limited region in radar altimetery field.

In the next paragraph, we will refer only to the maximum of the return waveform when dealing with a fractal model.

4.2. Fractal topographic model

Following recent attempts to describe the topography of a planet surface by fractals, and several papers (Plaut and Garneau, 1999; Orosei et al., 2002) on the analysis of MOLA (Mars Orbital Laser Altimeter) data, from the Mars Global Surveyor spacecraft, a fractal model was introduced in our instrument performance evaluation. MOLA is a Laser Altimeter whose data can be reduced to topographic height and, due to the time interval between the measurements, have a horizontal surface measurement spacing Δx_0 of about 400 m.

Regarding the fractal profile, the properties we wish to remind briefly some of the peculiarities of the surface statistical parameters (Shepard et al., 1995; Shepard and Campbell, 1999). In particular, the RMS height depends on the length of the profile and this dependence can be expressed

by the following power law:

$$\sigma_z(L) = [\langle (z-\bar{z})^2 \rangle]^{1/2} = \sigma_z(L_0)\left(\frac{L}{L_0}\right)^H \tag{28}$$

where H is the Hurst exponent and L_0 is the reference length.

The *Allan variance* (a measure of the difference in height between points separated by a distance Δx) and the *RMS slope* depends indeed on the step size Δx and in particular while the first increases with increasing step size the latter one decreases according to the relations:

$$v(\Delta x)^2 = \langle [z(x) - z(x+\Delta x)]^2 \rangle = v(\Delta x_0)^2 \left(\frac{\Delta x}{\Delta x_0}\right)^{2H}$$

$$= 2\sigma_z^2[1-\rho(\Delta x)], \tag{29}$$

$$s(\Delta x) = \frac{\sqrt{\langle [z(x) - z(x+\Delta x)]^2 \rangle}}{\Delta x}$$

$$= s(\Delta x_0)\left(\frac{\Delta x}{\Delta x_0}\right)^{H-1}. \tag{30}$$

The correlation coefficient is given (Shepard et al., 1995) by

$$\rho(\Delta x) = 1 - \frac{c^2}{k_s \sigma^2}|\Delta x|^{2H} \tag{31}$$

for stationary profile (i.e. the statistical properties of similar length segments are identical) $k_s = 2$.

Remembering the classical Gaussian and exponential correlation function, we can introduce the following:

$$\rho(\Delta x) = \exp\left(-\frac{|\Delta x|^{2H}}{L_f^{2H}}\right) \approx 1 - \frac{|\Delta x|^{2H}}{L_f^{2H}}. \tag{32}$$

The RMS slope obtained with the correlation coefficient given by Eq. (32) is shown in Fig. 1b. This result can be easily compared with what has been reported by (Plaut and Garneau, 1999) and (Orosei et al., 2002) (see Fig. 1a).

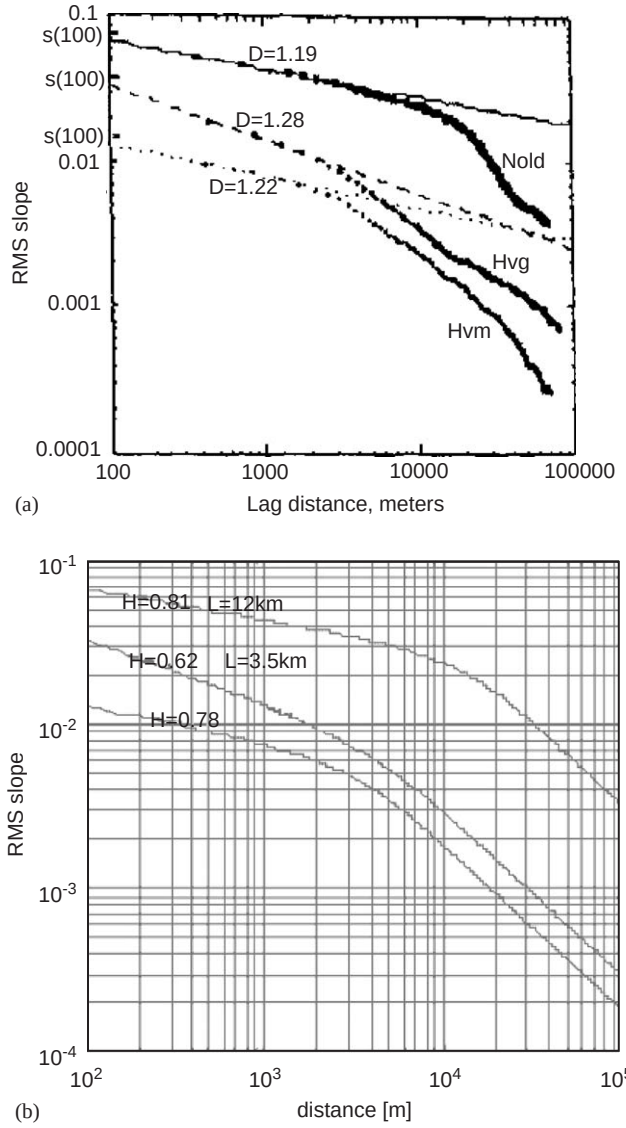

Fig. 1. RMS slope vs. lag distance obtained: (a) by (Plaut and Garneau, 1999); (b) with an exponential correlation function as given in Eq. (33).

4.3. Scattering end-models

The surface scattering and back-scattering terms can be evaluated by introducing a fractal geometric description of the surface and, as the worst case, in the classical Kirchhoff approximation of the scattered electric field from a random rough surface. Starting again from Eq. (12) with the same assumption that leads to Eq. (14), the backscattering cross-section, vs. scattering angle, can be written as (Biccari et al., 2001):

$$\sigma_0(\theta) = \frac{\Gamma_s(\theta)}{h\cos^2\theta}\left[\frac{(2\pi)^{(H-1)/H}}{[s(\lambda)]^{1/H}\sqrt{2}^{1/H}(\cos\theta)^{1/H}}\right]^2 \sum_{s=0}^{\infty}(-1)^s$$

$$\times \frac{\sin^{2s}\vartheta}{(s!)^2}\left[\frac{(2\pi)^{(H-1)/H}}{[s(\lambda)]^{1/H}\sqrt{2}^{1/H}(\cos\theta)^{1/H}}\right]^{2s}$$

$$\times \Gamma\left(\frac{s+1}{H}\right), \tag{33}$$

where $s(\lambda)$ is the surface *RMS slope* extrapolated at a scale equal to the wavelength, and $\Gamma(x)$ is the Gamma function. Eq. (33) gives, for $H = 1$, the geometric optics model, and, for $H = 0.5$, the well-known Hagfors model.

In fact in the case of $H = 1$ it is easy to obtain:

$$\sigma_0(\theta) = \frac{\Gamma_s(\theta)}{2m_s^2\cos^4\theta_0}\sum_{s=0}^{\infty}\frac{1}{s!}\left(-\frac{tg^2\theta}{2m_s^2}\right)^s$$

$$\equiv \frac{\Gamma_s(\theta)}{2m_s^2\cos^4\theta_0}\exp\left(-\frac{tg^2\theta}{2m_s^2}\right), \tag{34}$$

while for $H = 0.5$ it comes out:

$$\sigma_0(\theta) = \Gamma_s(\theta)\frac{C}{2}(\cos^4\theta + C\sin^2\theta)^{-3/2} \to C$$

$$= \frac{1}{(2\pi)^2 s^4(\lambda)}. \tag{35}$$

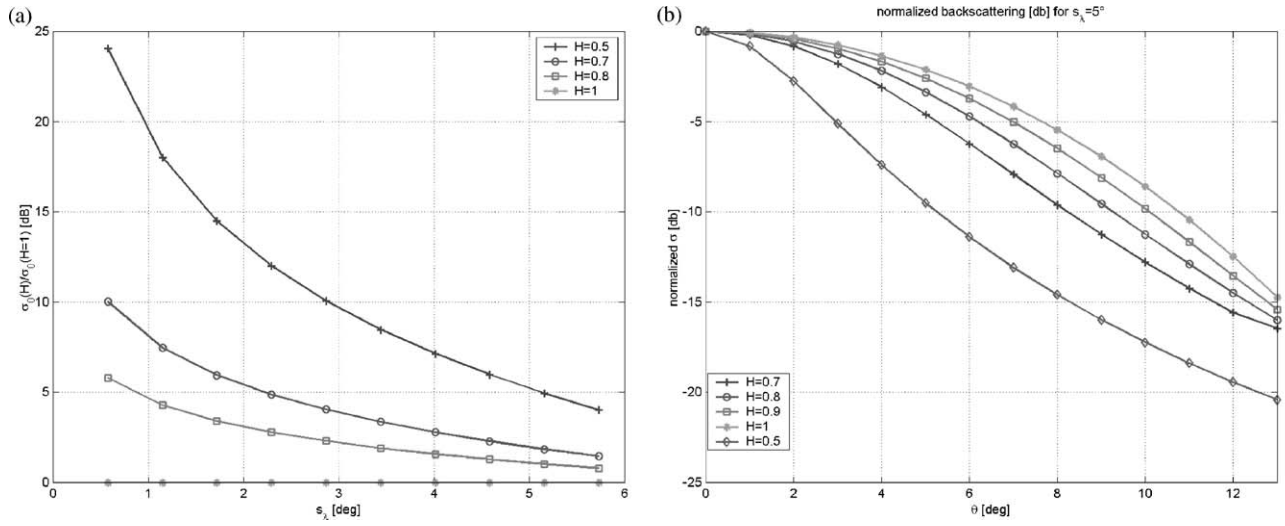

Fig. 2. (a) Backscattering at nadir angle vs. $s(\lambda)$ and for different values of H normalized to the backscattering computed for $H = 1$. (b) Backscattering for near nadir angle vs. ϑ for $s(\lambda) = 5^\circ$ and for different values of H.

Hence, we can consider as end models (s. normalized behaviour as shown in Fig. 2) the *geometric optics* and the *Hagfors* models.

Introducing now the orbital parameter and the subsurface depth we can write:

$$\sigma_0(\theta) = f(\theta) = f\left(\frac{r}{h}\right) = f\left(\sqrt{\frac{2z}{h}}\right) \to r$$

$$= \sqrt{2hz} \Rightarrow z_{ss} = \frac{z}{\sqrt{\varepsilon}} \tag{36}$$

where h is the orbiter altitude and r is the surface displacement referred to nadir point.

5. Signal/Clutter ratio estimation

The Subsurface Signal to Clutter (S/C) ratio vs. the Surface Signal to Clutter (S_1/C_1) can be written as

$$\left.\frac{S}{C}\right|_{\mathrm{dB}} \cong R_{12}|_{\mathrm{dB}} + \int_0^{z'} \alpha(z)\,\mathrm{d}z - \Gamma_s|_{\mathrm{dB}} + \left.\frac{S_i}{C_i}\right|_{\mathrm{SdB}}$$

$$= \alpha_{ss} + \left.\frac{S_i}{C_i}\right|_{\mathrm{SdB}} \tag{37}$$

assuming that the surface and the subsurface interfaces have the same roughness uncorrelated. Including the Doppler processing we obtain:

$$\frac{S_1}{C_1} = \frac{\int_{A_n} \sigma_0(\theta)\,\mathrm{d}A}{\int_{A_{on}} \sigma_0(\theta)\,\mathrm{d}A} = \frac{\int_0^{\sqrt{2h\delta}} f(\frac{r}{h})\,\mathrm{d}r}{f(\sqrt{2z'/h})(\sqrt{2h(z'+\delta)} - \sqrt{2hz'})}$$

$$\approx \frac{h}{\delta}\frac{\int_0^{\sqrt{2\delta/h}} f(x)\,\mathrm{d}x}{f(\sqrt{2z'/h})}\sqrt{\frac{2z'}{h}}, \tag{38}$$

where δ is the range resolution and z' is the depth.

When clutter is the limiting factor to the detection performance using the Eq. (37), we can obtain the maximum at which the subsurface echo can be detected against the surface clutter.

6. Detection of the ice/water interface with MARSIS

Taking into account the *Doppler beam sharpening* which is the Doppler processing in the along tack directions, and the results from Eq. (37) we can evaluate the maximum penetration depth of the MARSIS signal.

Table 6a shows the penetration depth of the signal, considering the I/W and D/I scenario, for a dynamic range 50 and 60 dB. This dynamic range can be reached if the signal to noise ratio estimate is met and the surface clutter is not the limiting factor in the detection (i.e. smooth surface with specular reflection).

Table 6b, show the detection depth calculated for different values of the surface RMS slope.

We can notice how the surface topography can strongly affect the radar penetration depth.

7. Conclusions

The main features of the MARSIS radar sounder and the expected subsurface sounding performance have been discussed, with respect to models of the Martian crust composition and topography as revealed from the analysis of MOLA data.

We have described the main features of the radar sounder and presented the expected penetration performance according to fractal models of the Mars crust, composition and geometric structure.

Table 6
MARSIS estimated detection depth in different subsurface scenarios. $s(\lambda)$ is the surface RMS slope extrapolated at a scale equal to the wavelength. H is the Hurst exponent: (a) dynamic range as limiting factor; (b) surface clutter as limiting factor

(a)

	ε'	$\tan\delta$	I/W Depth (km) (40 dB)	I/W Depth (km) (50 dB)	D/I Depth (km) (40 dB)	D/I Depth (km) (50 dB)
I	5	0.004	>5	>5	$4.4->5$	>5
II	9	0.03	1.1–1.8	1.5–2.2	0.8–1.3	1.1–1.8
III	7.1	0.014	2.1–3.3	2.8–4	1.6–2.5	2.3–3.3

(b)

	ε'	$\tan\delta$	I/W $H=1$ Depth (km) $s(\lambda)=0.1$	I/W $H=0.5$ Depth (km) $s(\lambda)=0.1$	I/W $H=1$ Depth (km) $s(\lambda)=0.06$	I/W $H=0.5$ Depth (km) $s(\lambda)=0.06$	I/W $H=1$ Depth (km) $s(\lambda)=0.03$	I/W $H=0.5$ Depth (km) $s(\lambda)=0.03$
I	5	0.004	<4	1.9–5.3	2.1–5.4	$5.3->6$	<4	1.9–5.3
II	9	0.03	<0.3	<0.5	<0.5	<1.2	<0.3	<0.5
III	7.1	0.014	<1	<1.5	<1.5	1.1–2.8	<1	<1.5

Considering the preliminary information available from the Mars Express science orbit with the constraints given by the solar zenith angle and data rate and the MOLA data and targets selected over Mars, the calculated sounding performances allow to optimize the operation planning and commanding by selecting the optimum operative mode.

References

Biccari, D., Picardi, G., Seu, R., Melacci, P.T., 2001. Mars surface models and subsurface detection performance in MARSIS. Proceedings of IEEE International Symposium on Geoscience and Remote Sensing, IGARSS 2001, Sydney, Australia, 9–13 July 2001.

Binder, A.B., Lange, M.A. 1980. On the thermal history, thermal state and related tectonism of a Moon of fission origin. J. Geophys. Res. 85,3194–85,3208.

Boynton, W.V., Feldman, W.C., Squyres, S.W., Prettyman, T., Brückner, J., Evans, L.G., Reedy, R.C., Starr, R., Arnold, J.R., Drake, D.M., Englert, P.A.J., Metzger, A.E., Mitrofanov, I., Trombka, J.I., d'Uston, C., Wänke, H., Gasnault, O., Hamara, D.K., Janes, D.M., Marcialis, R.L., Maurice, S., Mikheeva, I., Taylor, G.J., Tokar, R., Shinohara, C., 2002. Distribution of hydrogen in the near surface of mars: evidence for subsurface ice deposits. Science 297, 81–85.

Clifford, S.M., 1993. A model for hydrologic and climatic behaviour of water on Mars. J. Geophys. Res. 98, 10973–11016.

Ciaffone, A., Picardi, G., Seu, R., 1994. Application of the PARIS concept to the GPS signals. Technical Report #TR-1-3/1/95, STS Rome Italy, ESAcontract 142286-27/06/94.

Costard, F., Forget, F., Mangold, N., Peulvast, J.P., 2002. Formation of recent Martian debris flows by melting of near-surface ground ice at high obliquity. Science 295, 110–113.

Christensen, P.R., Morris, R.V., Lane, M.D., Bandfield, J.L., Malin, M.C., 2001. Global mapping of Martian hematite mineral deposits: remnants of water-driven processes on early Mars. J. Geophys. Res. 106, 23,873–23,885.

Fung, A.K., Eom, H.J., 1983. Coherent Scattering of a spherical wave from an irregular surface. IEEE, AP v. 31.

Fung, A.K., Li, Z., Chen, K.S., 1992. Backscattering from a randomly rough dielectric surface. IEEE, GE v. 30, n. 2.

Gaidos, E.J., 2001. Cryovolcanism and the recent flow of liquid water on Mars. Icarus 153, 218–223.

Gilmore, M.S., Phillips, E.L., 2002. Role of aquicludes in formation of Martian gullies. Geology 30, 1107–1110.

Grimm, R.E. Comparison of ground-penetrating radar and low-frequency electromagnetic sounding for detection and characterization of groundwater on Mars. Sixth International Conference on Mars, July 2003, Pasadena, CA, abstract no. 3176.

Malin, M.C., Edgett, K.S., 2000. Evidence for recent groundwater seepage and surface runoff on Mars science, 288 (5475) 2330–2335.

Mellon, M.C., Phillips, R.J., 2001. Recent gullies on Mars and the source of liquid water. J. Geophys. Res. 106, 23,165–23,179.

Mustard, J.F., Cooper, C.D., Rifkin, M.K., 2001. Evidence for recent climate change on Mars from youthful near-surface ground-ice. Nature 412, 411–414.

Orosei, R., Bianchi, R., Coradini, A., Espinasse, S., Federico, C., Ferriccioni, A., Gavrishin, A.I., 2002. Self-affine behavior of Martian topography at kilometer scale from Mars Orbiter Laser Altimeter data. J. Geophys. Res. 108 (E4) pp. GDS 4-1, Cite ID 8023, doi:10.1029/2002JE001883.

Picardi, G., Sorge, S., Seu, R., Fedele, G., Federico, C., Orosei, R., 1999. Mars Advanced Radar for Subsurface and Ionosphere Sounding (MARSIS): models and system analysis. Infocom Technical Report N.007/005/99.

Plaut, J.J., Garneau, S., 1999. MOLA-derived roughness data used to predict surface scattering for Mars subsurface radar sounding. The Fifth International Conference on Mars [CD-ROM], abstract 6239, Lunar and Planet. Inst., Houston, TX.

Shepard, M.K., Brackett, R.A., Arvidson, R.E., 1995. Self-affine (fractal) topography: surface parameterization and radar scattering. J. Geophys. Res. 100 (E6), 11,709–11,718.

Shepard, M., Campbell, B., 1999. Radar scattering from a self-affine fractal surface. Icarus 141, 156–171.

Ulaby, F.T., Moore, R.K., Fung, A.K., 1986. Microwave Remote Sensing: Active and Passive, Vol. II–III. Addison-Wesley, London.